Experimental study of bathymetry generated turbulence on tidal turbine behaviour

Benoît Gaurier, Maria Ikhennicheu, Grégory Germain, Philippe Druault

Experimental study of bathymetry generated turbulence on tidal turbine behaviour

Benoît Gaurier[a,*], Maria Ikhennicheu[a], Grégory Germain[a], Philippe Druault[b]

[a] *Ifremer, MetOcean Laboratory, 150 Quai Gambetta, 62 200 Boulogne-sur-mer, France*
[b] *Sorbonne Université, CNRS, UMR 7190, Institut Jean Le Rond d'Alembert, 75 005 Paris, France*

Abstract

In high flow velocity areas like those suitable for tidal applications, turbulence intensity is high and flow variations may have a major impact on tidal turbine behaviour. A three-bladed horizontal axis turbine model (scale 1:20) is positioned in the wake of a square wall-mounted cylinder, representative of specific *in situ* bathymetric variation, to experimentally study these effects in a current flume tank. Local and global loads are acquired in synchronisation with velocity measurements to study the turbine response to flow fluctuations. Velocity measurements need to be obtained close to the turbine, contrary to what is commonly considered, to properly correlate velocity and loads fluctuations. Results show that the loads phase average and their dispersion evolve according to the sheared velocity profile. We conclude that the turbine load fluctuations directly respond to the low frequency velocity fluctuations and are dominated by the turbulent structures shed from the cylinder. It is then possible to compare the effects of large coherent turbulent structures on the turbine behaviour to cases with more classical free stream turbulence commonly studied. These results provide a substantive database in high Reynolds number flows for further fatigue analysis or recommendations for turbine positioning in such flows.

Keywords: Turbulence, Experimental trials, Wall-mounted cylinder, PIV, LDV, Horizontal Axis Tidal Turbine

1. Introduction

Industrial projects for tidal energy harvesting have started to emerge all around the world. Understanding the impact that the extreme marine environment has on the survivability of tidal energy converters is fundamental for the successful development and commercialisation of full scale devices. Recent

*Corresponding author
Email addresses: benoit.gaurier@ifremer.fr (Benoît Gaurier), maria.ikhennicheu@ifremer.fr (Maria Ikhennicheu), gregory.germain@ifremer.fr (Grégory Germain), philippe.druault@sorbonne-universite.fr (Philippe Druault)

efforts from the scientific community to drive the development of tidal technology forward mainly include the estimation of wave loading on tidal energy devices [1, 2, 3, 4, 5, 6, 7]. According to Ouro et al. [8], energetic turbulent structures met in the tidal areas are the most relevant hydrodynamic features the marine turbines are subjected to. These structures are generated from irregular seabed bathymetry or large-scale turbulence that is convected with the free-stream flow. In such tidal areas, turbulence intensity varies between 3 % and 24 % [9] and many papers have underlined the importance of studying the turbulent inflow impacting the turbines, e.g. Refs. [10, 11] for wind turbines. Among these studies, some of them have been carried out in the IFREMER flume tank: e.g. see Refs. [9, 12, 13, 14]. Mycek et al. [9] concluded that the wake of a tidal turbine is dissipated faster when the inflow turbulence intensity increases. Blackmore et al. demonstrated in Refs. [15, 12] that the increase of turbulence intensity and turbulent length scale slightly increases the power and thrust coefficients. Durán Medina et al. [13] as well as Payne et al. [14] showed that the flow turbulence intensity significantly affects the temporal variability of the turbine power production. Another consequence is the impact of these velocity fluctuations on the structural loads or on the blade fatigue which has been studied by Davies et al. [16] for instance. Finally, the temporal power variability due to turbulent flow presents a major challenge for electrical grid systems, as shown by Lewis et al. [17].

A better understanding of the nature of turbulence in tidal areas is therefore a key goal in the successful installation and operation of tidal energy devices. Understanding the structure of turbulence will make it possible to predict its appearance and possibly manage or control its influence. The design of modern marine current turbines is currently being driven by the extreme loads imposed upon the turbine. As noted by Madsen et al. [18], these extreme loads during normal operation in turbulent conditions may exceed the design loads for wind turbine.

The study of Kelley et al. [10] underlines the importance of the coherence level of the incoming flow for fatigue loads analysis. Churchfield et al. [11] studied a wind turbine submitted to a stable and unstable flow with a high or low surface roughness. They concluded that coherent turbulent structures embedded in the flow cause loads fluctuations as significant as when the turbine is in the wake of another upstream turbine. The study of Chamorro et al. [19] focuses on an experimental set-up where a vertical cylinder produces Von-Kármán vortex streets that impact the turbine afterwards. They showed that the loads are impacted in the same frequency range as the vortex emitted from the cylinder wake. Byrne et al. [20] showed that if obstacles, with a size of more than 20 % of the turbine size, occupy more than 30 % of the turbine swept area, the turbine must be elevated or its location changed to avoid any structural issue. Chamorro et al. [21] underline the lack of study on the turbulent structures effect on turbines power production and wake meandering, especially for bathymetry generated structures. One of the most extended studies on that topic is the

paper written by Ouro et al. [8] where the behaviour of a turbine above dunes is numerically studied at $R_e = 6 \times 10^4$, with a focus on the turbine wake. Fatigue analysis exists on tidal turbine blades submitted to fluctuating loads in a marine environment, e.g. see Refs. [16, 22]. However, no fatigue study was found with loads fluctuations from large scale turbulent structures emitted from bathymetry elements.

Ikhennicheu et al. [23] present a case study comparison of various elementary obstacles used to reproduce bathymetry variations, like those encountered in the Alderney Race (middle of the English Channel), as shown by its geological description by Furgerot et al. [24]. They concluded that wide obstacles (6 times wider than its height) produces the most energetic wake that extends up to the free surface. In this case, large scale turbulent structures are periodically emitted from its wake and their diameter is similar to the one of a turbine at the same scale [25]. In order to know if such flow structures can be critical for tidal turbines behaviour, specific studies must be carried out. This work proposes to extend the existing database of the literature with the experimental study of a turbine response to the coherent turbulent wake of a wall-mounted square cylinder at a high Reynolds number of $R_e = 2.5 \times 10^5$.

The experimental set-up is described first with a presentation of the tank, the velocimetry techniques and the three-bladed horizontal axis turbine model. Then, the flow variations characteristics are detailed. The impact of this particular inflow on the turbine behaviour is finally investigated through the analysis of local and global loads, correlation and coherence studies.

2. Experimental set-up

2.1. Flume tank and instrumentation

The tests have been carried out in the wave and current circulating flume tank of IFREMER located in Boulogne-sur-mer (France) presented in Figure 1. The test section is 18 m long $\times$ 4 m wide $\times$ 2 m high.

In this work, the three instantaneous velocity components are denoted (u, v, w) along the (x, y, z) directions respectively. x is the main flow direction, y is oriented from the observation window towards the wall and z is from the tank bottom to the free surface (see Figure 4). Each instantaneous velocity component is separated into a mean value and a fluctuating part according to the Reynolds decomposition: $u = \overline{u} + u'$, where an overbar indicates the time average. The incoming flow $(u_\infty, v_\infty, w_\infty)$ is assumed to be steady and constant. By means of a grid and a honeycomb, that acts as a flow straightener, placed at the inlet of the working section, a turbulent intensity of $I_\infty = 1.5$ % is achieved for a flow velocity of 1 m/s. Turbulence intensity I_∞ in the incoming flow is defined by equation 1, with σ the standard deviation.

$$I_\infty = 100\sqrt{\frac{\frac{1}{3}(\sigma(u_\infty) + \sigma(v_\infty) + \sigma(w_\infty))}{\overline{u_\infty}^2 + \overline{v_\infty}^2 + \overline{w_\infty}^2}} \tag{1}$$

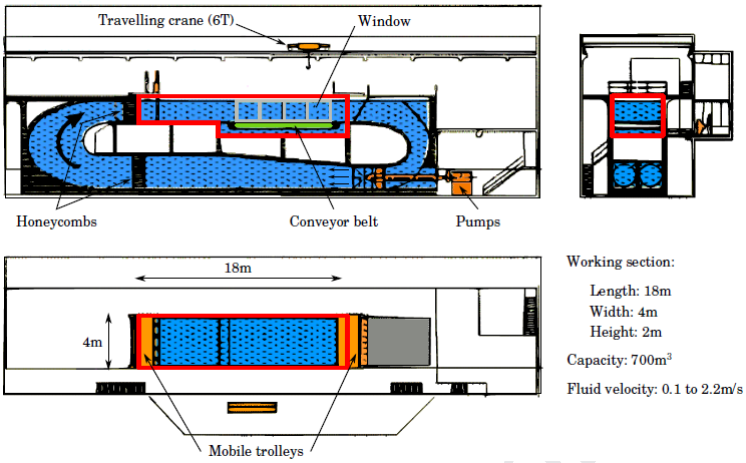

Figure 1: Schematic of the IFREMER flume tank

The obstacle considered here is a wall-mounted cylinder, chosen to be representative of a wide obstacle in real-life conditions. Such obstacle can be observed in the Alderney Race (English Channel) according to its geological description by Furgerot et al. [24], which is a suitable area for tidal turbines installation. Its dimensions are $H \times 6\ H \times H$, with H the obstacle height. The upstream flow is a simple boundary layer developing over the tank floor. At the obstacle position, the boundary layer height δ is calculated as $\delta_{95} = z(0.95 \times \overline{u_\infty})$. It yields $\delta = 0.325\ m$. To consider turbulent events interaction with the free surface, experiments are achieved in Froude similitude where $F_r = \dfrac{u_\infty}{\sqrt{gD_b}}$, with g the gravity and D_b the tank depth. Furthermore, obstacle height H is chosen to be high enough so that the Reynolds number is close to real conditions and low enough to limit the blockage ratio: $R_e = \dfrac{Hu_\infty}{\nu}$ with ν the water viscosity. It yields $H = 0.25\ m$ (see Table 1 for all dimensions). In the following, non dimensional lengths are used for all parameters indexed by *: $x^* = x/H$, $y^* = y/H$, $z^* = z/H$ and $\delta^* = \delta/H$.

Table 1: *In-situ* and experimental conditions (1:20 scale): u_∞ stands for the far upstream velocity, H for the rugosity height, D_b for the water depth, R_e for the Reynolds number, F_r for the Froude number and D for the turbine diameter.

	Scale [-]	u_∞ $[m/s]$	H $[m]$	D_b $[m]$	R_e [-]	F_r [-]	D $[m]$
Alderney Race	1	5	5	40	2.5×10^7	0.25	$\simeq 15$
Flume tank	1/20	1	0.25	2	2.5×10^5	0.23	0.724

To characterize the flow, two Laser Velocimetry techniques are used: LDV (Laser Doppler Velocimetry) and PIV (Particle Image Velocimetry). Beforehand, the water of the tank is seeded with 10 μm diameter silver coated glass

micro-particles.

For the PIV measurements, a Nd-YAG Laser GEMINI-LIKE is used: power is 200 mJ per probe and wavelength is 532 nm. The laser is synchronized with a Camera FLOWSENS EO-2M 1600 pix $\times$ 1200 pix which acquires double images with a time lag of 1600 μs. PIV measurements are acquired during 180 s, hence 2700 double images are taken with an acquisition frequency $f_e = 15\ Hz$. The data are post processed with the software DYNAMIC STUDIO. The displacement of particles is calculated using a Cross-Correlation on 32 pix $\times$ 32 pix interrogation windows with 50 % overlap [26]. Outliers are detected using the Universal Outlier Detection method [27].

The LDV measurements are carried out using a 2D DANTEC FIBERFLOW system. The probe is positioned horizontally for (u, v) measurements. With LDV measurements, the acquisition frequency is not constant. It depends on the number of particles passing through the measurement volume. At a specific streamwise position, f_e varies from 200 to 300 Hz depending on the turbulent agitation and the flow velocity.

Various sources of experimental errors can be identified for both techniques, they are detailed in [25].

A three-bladed horizontal axis turbine (Figure 2) is positioned in the cylinder wake. This turbine has been developed at IFREMER and was first presented in [28]. The turbine blades are rigid and their open geometry is described in [9, 29]. Its diameter is $D = 0.724\ m$ (Table 1). The turbine rotation speed is controlled and the blade pitch does not change. Each blade root is equipped with a specific load-cell including 5 different channels: 2 forces (F_{xi} and F_{yi}) and 3 moments (M_{xi}, M_{yi} and M_{zi}, $i = 1, 2, 3$). Blades axis are detailed in Figure 3. The torque (M_{tot}) and the thrust (F_{tot}) applied on the main rotation axis are also measured.

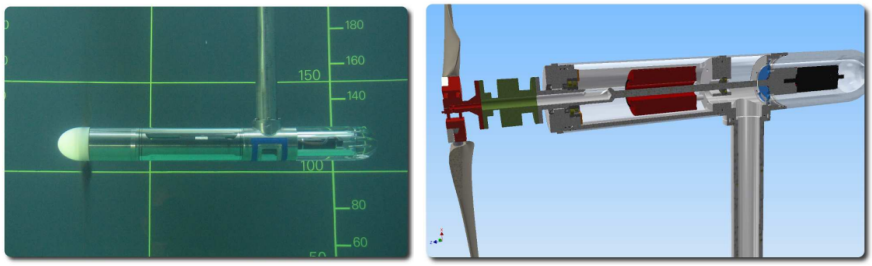

Figure 2: Picture and schematic side view of the experimental turbine

This turbine is positioned at mid-depth in the tank and at a distance $x^* = 16$ from the cylinder. The experimental set-up is represented in Figure 4 and depicted on Figure 5 To characterise the turbine load fluctuations, the incoming velocity is measured in two different ways:

1. with a single LDV point, located $2D$ upstream of the turbine and at the hub height ($z^* = 4$), acquired in synchronization with the turbine loads.

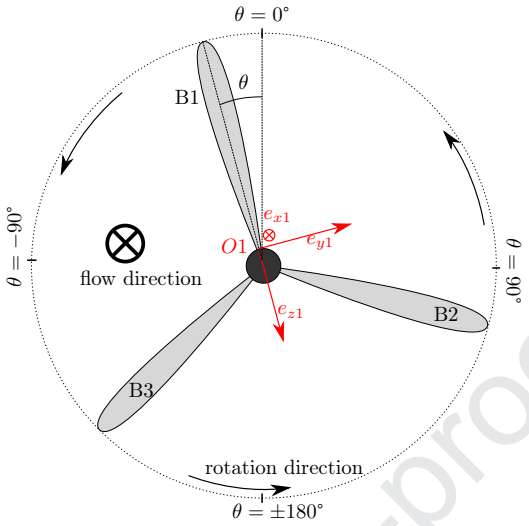

Figure 3: Representation of the blades axis and rotation direction of the turbine facing the flow with angular positions

This upstream distance ($2D$) is commonly used in the literature (e.g. see Ref. [30]). Its pertinence is however discussed in Ikhennicheu et al. [25] and in the present study.

2. with a PIV map, located as close as possible to the turbine rotor and in the plane (XOZ). The size of the PIV map is $330 \times 840\ mm^2$. It is centred vertically at the hub height and ends horizontally at the blade root. It is acquired in synchronization with the turbine loads as well.

Both velocity measurement techniques are not acquired simultaneously since the LDV probe immersed in the water would create perturbations in the PIV plane. LDV and PIV characteristics are summed up in Table 2.

Velocimeter	Probe plane position	f_e $[Hz]$	Duration $[min]$
PIV	$x^* = 16 - 0.2 = 15.8$	15	3
LDV	$x^* = 16 - 2D/H = 10.4$	$[200; 300]$	6

Table 2: Sum up of the incoming flow measurements carried out upstream from the turbine

In this study, the turbine is considered parked (TSR0) or rotating. The rotation speed is chosen as the nominal operating point, which corresponds to the turbine highest produced power. In the present set-up for which the Tip Speed Ratio (TSR) similitude is used, that point is $TSR = 4$ (TSR4), as shown in Gaurier et al. [29]. It is reminded that $TSR = \dfrac{\Omega R}{u}$ with Ω the angular velocity and $R = 0.362\ m$ the turbine radius.

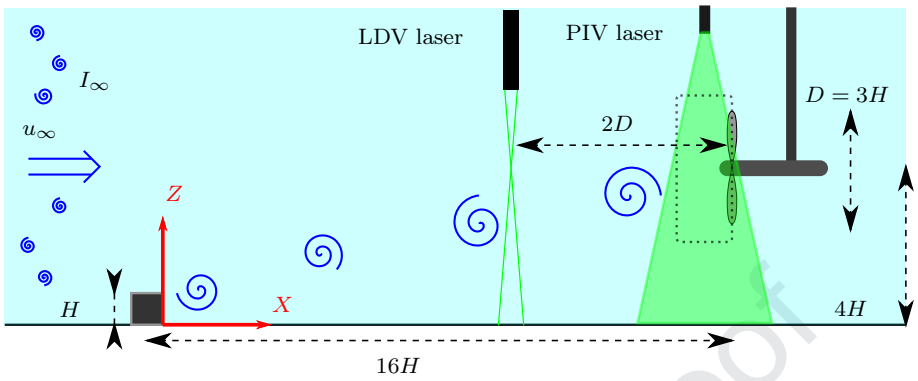

Figure 4: Schematic representation of the experimental set up with the cylinder of height H and the turbine with diameter D. The incoming flow with its far velocity u_∞ and turbulence intensity I_∞ is characterized upstream of the turbine with PIV and LDV measurements. Both velocity measurement techniques are not acquired simultaneously, but always in synchronization with the turbine loads. Dotted rectangle indicates the PIV camera field of view.

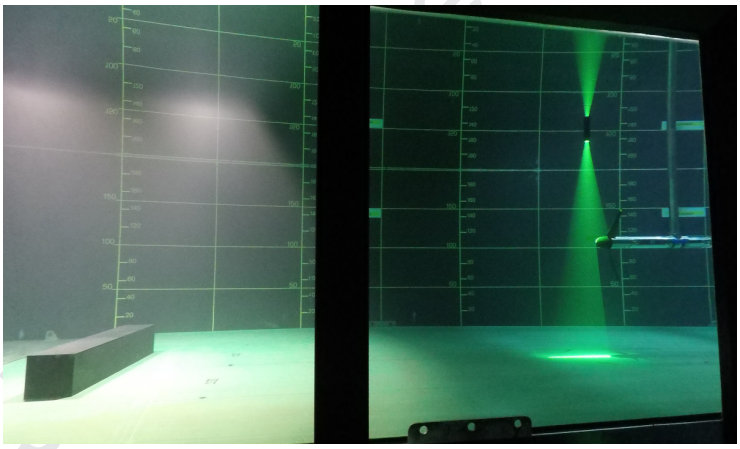

Figure 5: Picture of the set up in the tank: the upstream cylinder with PIV laser shooting in front of the turbine

2.2. Inflow characterization

The cylinder wake, described in Ikhennicheu et al. [25], is represented on Figure 6. It extends towards the surface so that the turbine is half immersed in the wake of the obstacle, at $x^* = 16$. The standard practice of measuring velocity $2D$ upstream of the turbine ($x^* = 10.4$) is compromised here. Indeed, due to the rising nature of the wake, the velocity changes between the LDV measurement point and the turbine position (PIV measurement position). Here, there is a 10 % difference on the average velocity and a 45 % difference on the standard deviation between the two locations: $\sigma(u_{LDV}) = 0.07$ and $\sigma(u_{PIV}) = 0.13$.

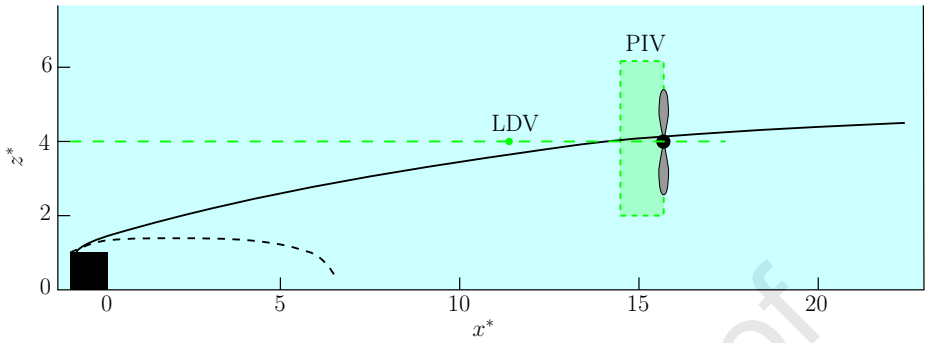

Figure 6: Representation of the cylinder wake extension versus the turbine location. The full black line represents the wake extension: $\overline{u} = 0.9 \times \overline{u}_\infty$. The dotted black line stands for the recirculation zone: $\overline{u} < 0$. The positions of the laser measurements (LDV and PIV) are displayed as well.

The velocity profiles measured with PIV at 0.2 H upstream of the turbine are presented on Figure 7 over the turbine diameter. Cases with and without the turbine which is in rotation or parked are displayed. Without the turbine, the velocity profile illustrates that the cylinder wake (where $\overline{u} < 0.9 \times u_\infty$) reaches $z^* \simeq 4.5$ (Figure 7**a**). Above that position, the average velocity and turbulent intensity of the outer flow is restored: $\overline{u} = u_\infty$ and $I = I_\infty$. There is a strong average velocity difference between the top and the bottom of the profile (0.23 m/s). That velocity difference is relevant because even though it has low influence on the turbine global performance, it strongly impacts the loads variability on each blade according to Li et al. [31]. There is also a difference of around 50 % in the standard deviations between the top and the bottom of the velocity profile.

The turbine presence induces a strong inflow velocity deficit of around 20 % at hub height, between the no turbine case and the TSR0 case (Figure 7**b**). An inflexion of the velocity profile is clearly noticeable close to $z^* = 4$ as well. Indeed, the momentum theory shows that the flow speed reduces from the freestream conditions far upstream of the turbine to the velocity incident at the rotor plane. That effect leads to the apparition of an induction zone upstream of the turbine as explained by Simley et al. [32] for a full-scale wind turbine. When the turbine rotates, the velocity deficit increases (Figure 7**c**). With the parked turbine, since blade 1 is at the top dead centre, the velocity in the top part of the profile upstream of the blade reduces. At the profile bottom part, i.e. for $z^* < 3$, blades 2 and 3 are out of the measurement plane, hence the velocity profile is identical to the one in the empty tank (Figure 7**d**). With the turbine at TSR4, the velocity decrease is visible on the whole velocity profile.

The spectral content of the cylinder wake is extensively described in Ikhennicheu et al. [25] showing large scale vortices shed downstream of the obstacle at a frequency around 0.3 Hz Figure 8 presents the velocity spectral content upstream of the rotating turbine. The Power Spectral Density, S_{uu} and S_{ww}

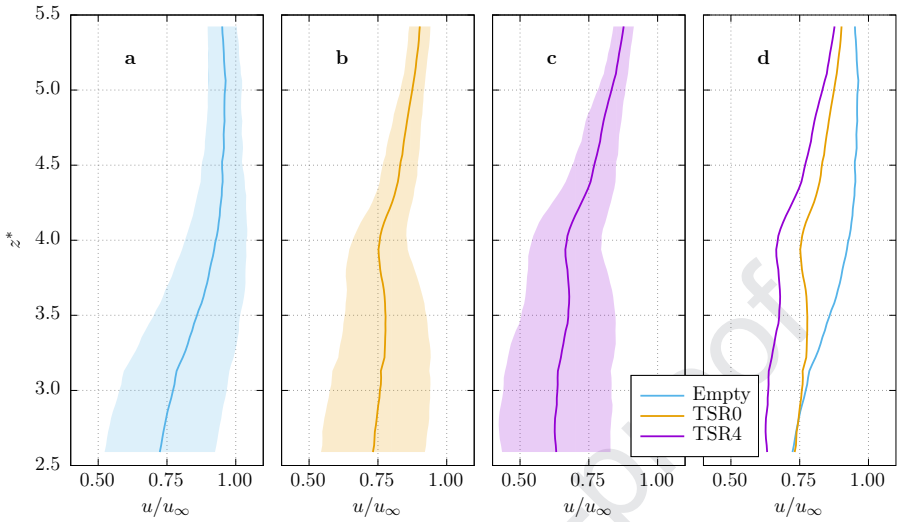

Figure 7: Vertical profiles of the average and standard-deviation of the streamwise component of the normalised velocity u/u_∞, from the PIV measurements at $x^* = 15.8$ behind the obstacle. Cases without turbine (**a**) and with the turbine parked (**b**) and rotating (**c**) are displayed with the superposition of all time-averaged profiles (**d**) for an easier comparison. The vertical range of the plots corresponds to the turbine diameter, i.e. $z^* \in [2.55; 5.45]$, $z^* = 4$ being the centre of rotation.

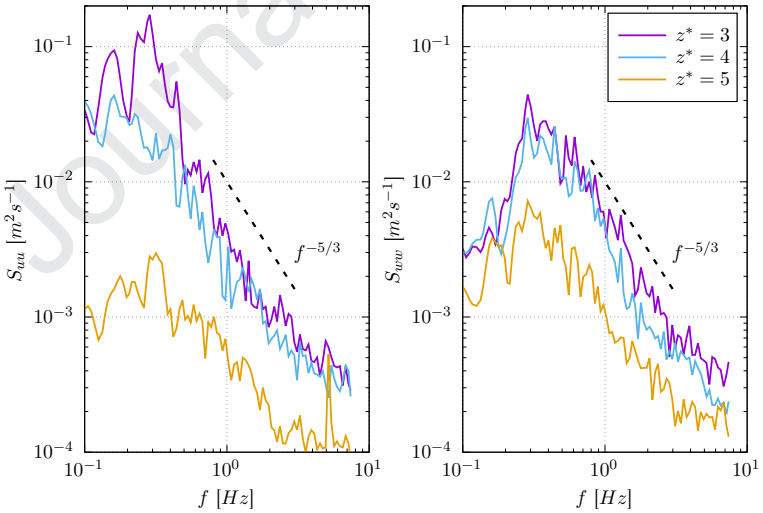

Figure 8: Power Spectral Density (S_{uu} and S_{ww}) of the streamwise u and spanwise w components of the velocity, at three different depths $z^* = [3; 4; 5]$, from the PIV measurements at $x^* = 15.8$ behind the obstacle, with the turbine rotating at TSR4. The main peak at $f \simeq 0.3\ Hz$ correspond to the vortex shedding from the cylinder. The peak at $f \simeq 5.4\ Hz$ corresponds to the turbine blade passing frequency. These spectra follow a $-5/3$ power slope.

for the streamise and spanwise components of the velocity, enables two peaks to be identified:

- at $f \simeq 0.3\ Hz$, with a high amplitude, corresponding to the shedding frequency coming from the cylinder,
- at $f \simeq 5.4\ Hz$, with a relatively low amplitude, equals to 3 times the rotation frequency ($f_r = 1.8\ Hz$ at TSR4). This is the blade passing frequency.

This last frequency is mainly noticeable at $z^* = 5$. Hence, at $x^* = 15.8$, the flow is submitted to the obstacle vortex shedding and the blade shadowing effect (0.2 H downstream of the PIV map). The vortex structures contained in the upstream flow interact with the turbine, modifying their behaviour close to the turbine position. In the following, we study the turbine response to the vortex structure impacts.

3. Turbine response characterization

3.1. Turbine response to velocity fluctuations

In this section, the rotor loads are analysed. Loads averaged values and standard deviations are given in table 3 for the thrust F_{tot} and local loads on each blade. When the turbine is in rotation at TSR4, loads values are $F_{xi} > 0$ and $F_{yi} < 0$ ($i = 1, 2, 3$) which is consistent with the turbine rotation direction (see Figure 3) and the sensors orientation. For the parked turbine, average and standard-deviations values follow the same trend as the rotating case but they are about 50 times lower. A difference appears between the blades loads, especially on the F_{xi} where the standard deviation on blade 1 is 2.5 lower than for blades 2 and 3. Indeed, without rotation, the turbine remains in its initial position: blade 1 is at the top dead centre and blades 2 and 3, shifted of $\pm 120°$, out of the symmetry plane. The turbine is half immersed in the cylinder wake and the velocity fluctuations present in the wake only impact the lower part of the turbine. With the rotation, the blades are periodically immersed in the wake and the local load average is the same on all three blades. Minimal and maximal values indicate thrust fluctuations ranging up to 25 % of the average values underlining how critical that test case could be for turbine structural integrity.

In order to study the turbine response, vortices present in the cylinder wake are presented, based on the observations from Ikhennicheu et al. [25]. Figure 9a presents a fluctuating velocity field of an ideal vortex, illustrating the local acceleration on its bottom part and the deceleration on its top part. Comparing these two vortices, the one observed on the PIV field is vertically asymmetrical around its centre (see Figure 9b). Hence, only the significant deceleration in the bottom part of vortices is likely to be perceived by the turbine.

	F_{tot}	F_{x1}	F_{x2}	F_{x3}	F_{y1}	F_{y2}	F_{y3}
				TSR0			
Average value	37.0	11.2	10.3	10.4	-2.0	-2.4	-1.9
Standard-deviation	4.3	0.8	1.9	1.9	0.2	0.4	0.4
Min. value	11.4	4.2	1.8	0.8	-3.5	-4.7	-3.8
Max. value	49.7	15.2	15.2	15.2	-0.5	-0.7	-0.2
				TSR4			
Average value	178.0	55.0	56.2	54.5	-11.4	-14.7	-8.6
Standard-deviation	19.1	9.0	9.0	9.0	3.6	3.7	3.7
Min. value	58.9	1.6	8.8	8.2	-21.7	-27.7	-20.9
Max. value	221.6	74.6	74.6	74.6	3.3	1.5	6.1

Table 3: Average, standard-deviation, minimum and maximum values of the turbine local loads (F_{xi} and F_{yi}) and thrust (F_{tot}), expressed in N, recorded for turbine at TSR0 and TSR4

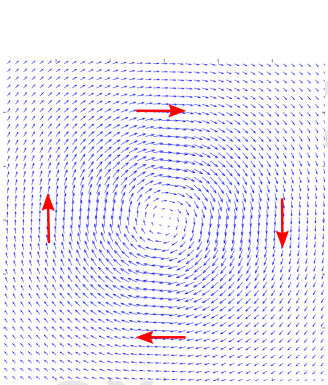

(a) Ideal vortex

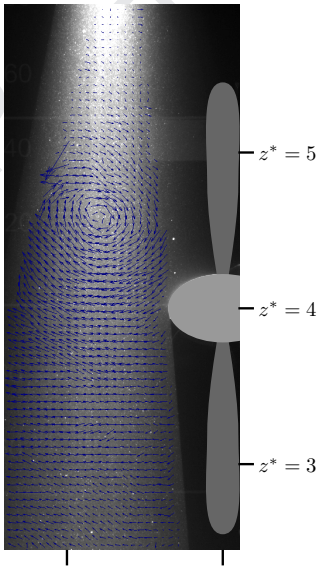

(b) Instantaneous fluctuating velocity field

Figure 9: Schematic representation of an ideal vortex and picture of the laser lighting the particles upstream of the turbine at TSR4, superimposed with the instantaneous fluctuating velocity field. A drawing of the turbine has been added on the picture to highlight its position. Comparing the ideal vortex with the measured field, the vertical asymmetry of the fluctuating velocity is noticeable.

The fluctuating parts of the time evolution of the streamwise component of the velocity $u'(x^* = 15.8, t)$ as well as the turbine loads F'_{tot} and F'_{xi} are

presented on Figure 10, for the parked turbine (TSR0). These velocity signals are extracted from the PIV acquisitions, at three altitudes $z^* = [3; 4; 5]$, for a specific time range. At $t = 19.5\ s$, a vortex passes in the PIV measurement plane and induces a strong velocity deficit for $z^* \leq 4$. This depth corresponds to the lowest part of the vortex, hence a strong deceleration. At the same time, the top part of the vortex ($z^* = 5$) presents a slight acceleration, which is however too low to be considered. Consequently, F'_{tot}, F'_{x2} and F'_{x3} show a decrease of about 15 N and 6 N respectively, corresponding to the instantaneous deceleration induced by the vortex passing. F'_{x1} does not fluctuate much in comparison. Indeed, for the parked turbine, blade 1 is at the top dead centre and is thus not immersed in the wake.

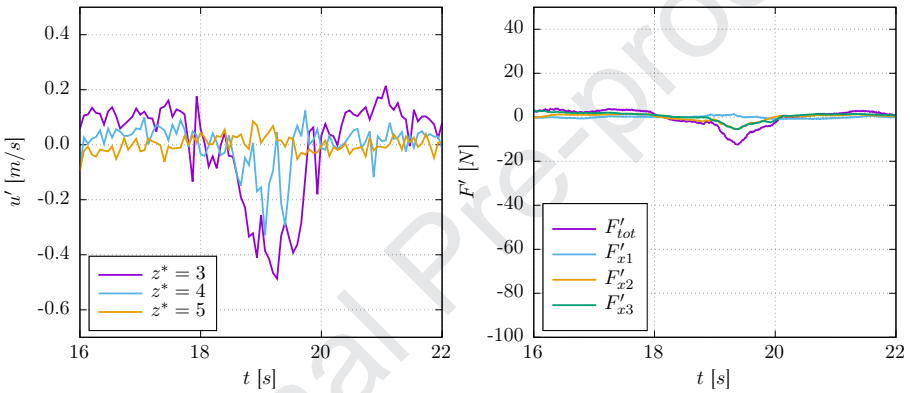

Figure 10: PIV extracted streamwise velocities at 3 different depths $z^* = [3; 4; 5]$ (left) and time-corresponding turbine loads fluctuation signals (right), measured when the turbine is parked (TSR0). The range of the loads fluctuation is deliberately large to be consistent with the following figure 11.

The fluctuating parts of the time evolution of the streamwise component of the velocity $u'(x^* = 15.8, t)$ as well as the turbine loads F'_{tot} and F'_{xi} are presented on Figure 11, for the rotating turbine at TSR4. Some particular events: $t_1 = 12.8\ s$, $t_2 = 16.8\ s$, $t_3 = 19.8\ s$, $t_4 = 24.4\ s$ and $t_5 = 28.0\ s$ are identified and two of them are analysed using the instantaneous fluctuating velocity fields in Figure 12. In the case of vortices at t_1, t_3 and t_5, a local velocity deceleration ($\simeq -0.4\ m/s$) is detected for $z^* = 3$ and $z^* = 4$, excepted at t_3 where a local acceleration is detected for $z^* = 4$. These three events correspond to vortices whose centre passes at the turbine height and for which the strong deceleration of the bottom part is detected (figure 12**a**). Vortices at t_1, t_3 and t_5 are of the same type as the one illustrated in Figure 9b. They are very energetic and their rising angle is particularly high [25]. Concerning events at t_2 and t_4, a quick variation of the velocity amplitude (deceleration and acceleration of $\simeq 0.2\ m/s$) is detected for the lowest position only ($z^* = 3$). These events correspond to the bottom part of low intensity vortices whose centre passes around the bottom of the turbine (figure 12**b**).

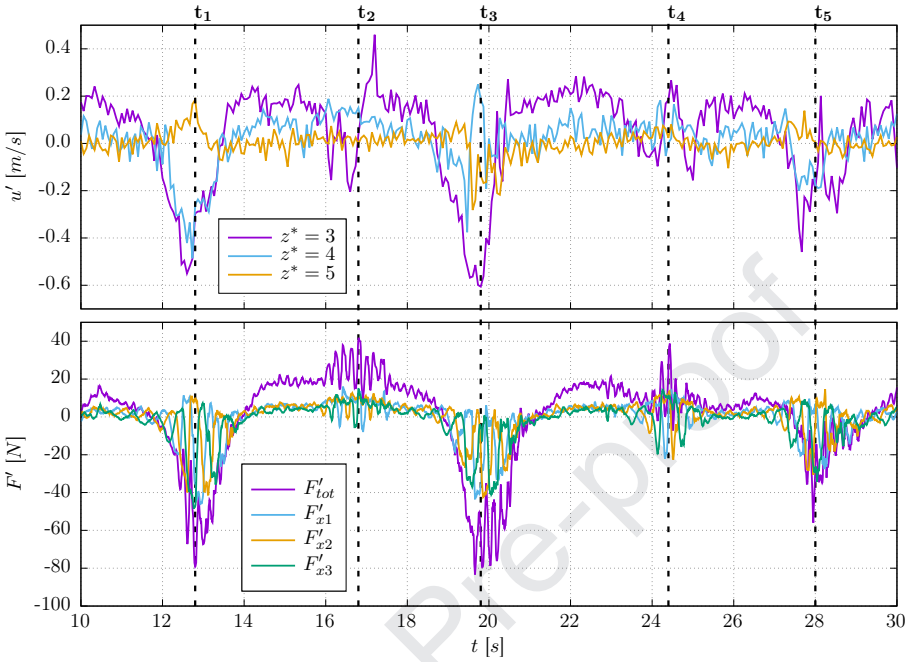

Figure 11: PIV extracted streamwise velocities at 3 different depths $z^* = [3; 4; 5]$ (top) and time-corresponding turbine loads fluctuation signals (bottom), measured when the turbine is at TSR4. Times t_1 to t_5 emphasis particular events described in the text. Instantaneous PIV fluctuating velocity fields corresponding to time events t_1 and t_2 are displayed on figure 12.

The turbine loads show periodic fluctuations at the rotation frequency. The amplification of these fluctuations corresponds to the instantaneous increase of the shear in the velocity profile when a vortex passes. That effect is considerable [31] and has to be considered for fatigue analyses [16, 22]. At t_1, t_3 and t_5, local velocity decelerations cause loads diminutions of about 80 N for the global thrust and about 40 N for the F_{xi}, due to high energy vortices passing at the rotation axis turbine depth. Comparing to the previous case for the parked turbine, similar vortices induce loads variations with magnitude about 6 times higher. At t_2 and t_4, the amplitude of the velocity fluctuations are low and the corresponding loads fluctuations do not decrease. However, the vortex presence still induces an instantaneous shear increase. Consequently, loads fluctuations at the turbine rotation frequency is clearly noticeable with amplitude of 20 to 10 N for the thrust and local loads respectively. Hence, the turbulent events, generated in the cylinder wake, strongly impact the turbine local and global loads. That effect is also observed by Ouro et al. [8] behind dunes from which large scale structures are also emitted.

Cross-correlation is then used to determine the similarity between the flow velocity u and the rotor load F_{tot}. The normalized cross-correlation between

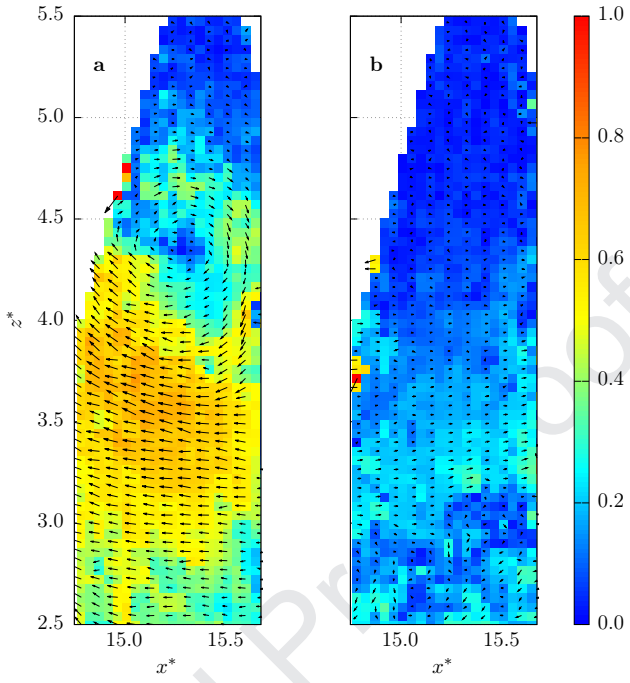

Figure 12: Instantaneous fluctuating velocity fields measured by PIV upstream of the turbine position (blades are at $x^* = 16$), when the turbine is in rotation at TSR4 and for events corresponding to time t_1 (**a**) and t_2 (**b**), as depicted on Figure 11. Colours correspond to the norm of the fluctuating velocity, i.e. $\sqrt{u'^2 + w'^2}$, expressed in m/s.

these signals is evaluated as follows:

$$R_{uF_{tot}}(\tau) = \frac{1}{\sigma(u)\sigma(F_{tot})} \sum_{i=1}^{N} u'(t_i + \tau) F'_{tot}(t_i) \tag{2}$$

The normalized cross-correlations between the streamwise velocity u and the turbine global thrust F_{tot} are compared in Figure 13**a** for both measured velocity devices: LDV at $x^* = 10.4$ and $z^* = 4$ and PIV at $x^* = 15.8$ and $z^* = 4$. The time lag τ is higher for the LDV measurement because it is further away from the turbine comparing to the PIV measurement. The correlation peak is more elevated for PIV compared to LDV: $R_{uF_{tot}} = 0.70$ compared to $R_{uF_{tot}} = 0.45$. Indeed, the LDV measurement is located too upstream to account for velocity fluctuations that may impact the turbine (see Figure 4). Hence, in the case of a turbine immersed in the wake of a bathymetric obstacle, velocity measurements need to be achieved as close as possible to the turbine to be able to correlate the loads and the velocity fluctuations. In the rest of the study, PIV measurements is used for correlation and coherence studies.

Correlation is then compared between the turbine at TSR0 and TSR4 in Figure 13**b**. Correlation is slightly lower for the parked turbine. Without rota-

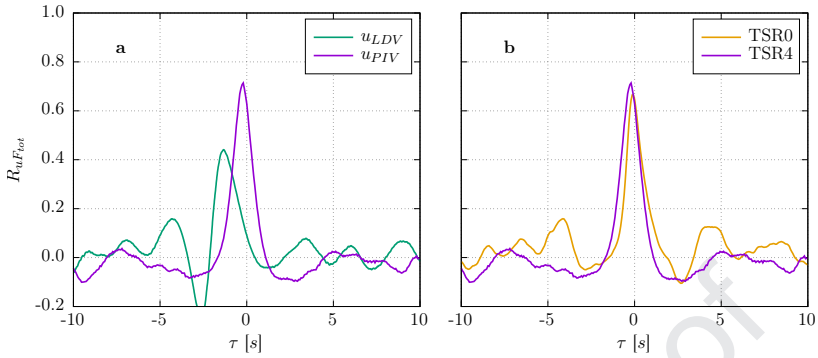

Figure 13: Correlation $R_{uF_{tot}}$ between the streamwise velocity and the global turbine thrust: **a** with turbine at TSR4 using PIV and LDV measurements and **b** using PIV measurements only with turbine at TSR0 and TSR4. The PIV point is extracted from the measurement field at the location $x^* = 15.8$ and $z^* = 4$ whereas the LDV point is located at $x^* = 10.4$ and $z^* = 4$.

tion, blade 1 stays at the top dead centre, in the outer flow and is not impacted by the turbulent structures present in the wake. Hence, loads are not equal on the three blades. With the rotation, each blade receives similar velocity fluctuations. That effect is assumed to be responsible for the correlation increase between the parked and rotating turbine.

The previous section focuses on the instantaneous reaction of the turbine to velocity fluctuations. The average loads variations during one cycle of rotation contain important informations as well, especially for blades fatigue analysis as explained in the next section.

3.2. Loads angular evolution

The angular evolution of the turbine loads is now studied. An analytical method is developed to access the instantaneous turbine angle position θ, as illustrated in Figure 3. The fluctuating part of each blade force F_{yi} $(i = 1, 2, 3)$ is extracted and signals are filtered with a bandpass filter around the rotation frequency f_r. The weight of each blade is continuously measured by this force component and projected according to the turbine angle. For each blade, the resolution of an equation system enables θ_i to be processed. The turbine angle θ is then the average of the three θ_i. The difference between every processed θ_i is lower or equal to 1 %. A possible uncertainty source concerning this method is the temporal precision: when the turbine rotation speed is TSR4, the blade rotation is 5° between each time step, which can lead to an error of 2.5°. In the following, we study the angular repartition of the fluctuating part of the turbine loads as well as their corresponding phase averages, denoted $\widetilde{\square}$.

The fluctuating part of the bade 1 load force F'_{x1} and its phase average $\widetilde{F_{x1}}$ are represented on Figure 14, when the turbine is in rotation at TSR4. The

minimum and maximum of $\widetilde{F_{x1}}$ are reached at 149° and -29° respectively. We could have imagine that the highest value should have been found for $\theta = 0°$. This corresponds to the top of the velocity profile (see Figure 7), where the velocity is the highest. Such phase delay is already observed in [33, 14] in both numerical and experimental analysis in air or water. As explained by Dai et al. [34], turbine loads are influenced by many factors such as: interactions with the mast, the shear in the flow, dynamic stall on the blades and the turbine speed control system. Hence, considering the -30° phase delay observed on these results, the value of $\widetilde{F_{x1}}$ is consistent with the average velocity diminution between the top and the bottom of the velocity profile. Again, considering the phase delay of $-30°$, the highest dispersion of F'_{x1} values is located at the bottom position, due to the high turbulence level in the wake of the cylinder at the bottom of the velocity profile (see Figure 7). For the parked turbine (TSR0), blade 1 is at $\theta = 0°$ and blades 2 and 3 at $\theta = \pm 120°$. Standard-deviation of F_{xi} are then: $\sigma(F_{x1}, 0°) = 0.78\ N$, $\sigma(F_{x2}, -120°) = 1.9\ N$ and $\sigma(F_{x3}, 120°) = 1.9\ N$. Values at $\theta = \pm 120°$ are equal which shows that, without rotation, there is no phase delay. The parked turbine behaviour is thus symmetrical around the $\theta = 0°$ axis.

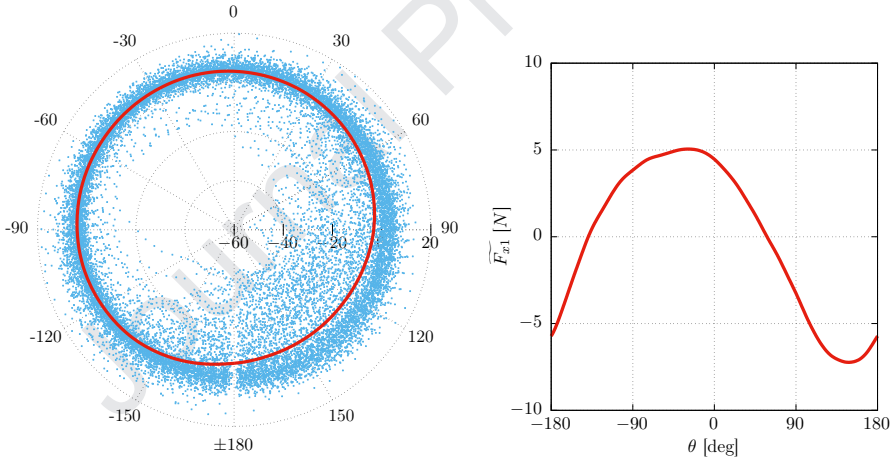

(a) (b)

Figure 14: Angular repartition of the fluctuating part of the bade 1 load force F'_{x1} (blue dots) when the turbine rotates at TSR4 and its phase average $\widetilde{F_{x1}}$ (red line), expressed in N. For a better visibility, $\widetilde{F_{x1}}$ is displayed on the polar plot (a) as well as on the Cartesian plot (b).

The phase average of the fluctuating component is studied for $\widetilde{F_{xi}}$, $\widetilde{F_{yi}}$ ($i = 1, 2, 3$) and $\widetilde{F_{tot}}$ on Figure 15. $\widetilde{F_{xi}}$ are rephased in Figure 15b: blade 1 is used as a reference and the origins of the values on blades 2 and 3 are reset by $\pm 120°$. This enables the illustration of the identical trend for all the blades. The sum of all the $\widetilde{F_{xi}}$ yields into the clover shape observed on Figure 15d for $\widetilde{F_{tot}}$, also observed by Payne et al. [14]. The rephased $\widetilde{F_{yi}}$ follow all the same trend (Figure 15c): the value is the highest at 90°, equal to 0 at 0°and 180°and the

lowest at 90°. This behaviour is consistent with a load depending on the blade weight only.

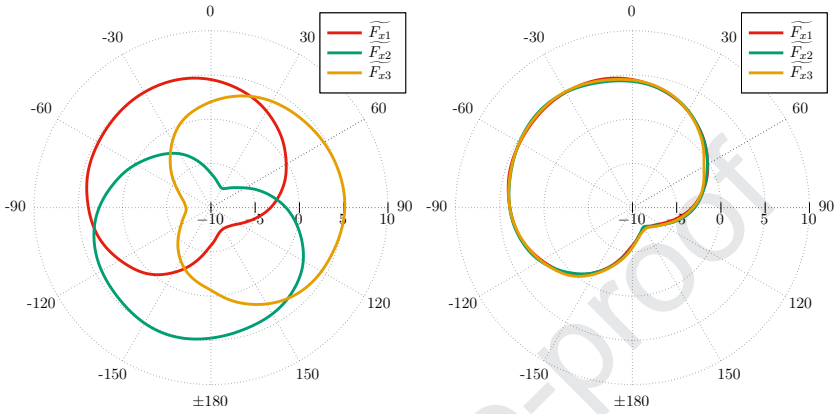

(a) $\widetilde{F_{xi}}$, $i = 1, 2, 3$

(b) $\widetilde{F_{xi}}$, $i = 1, 2, 3$, rephased

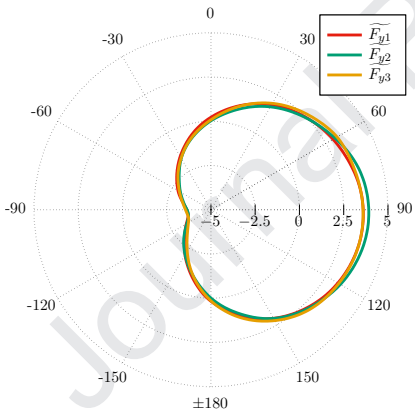

(c) $\widetilde{F_{yi}}$, $i = 1, 2, 3$, rephased

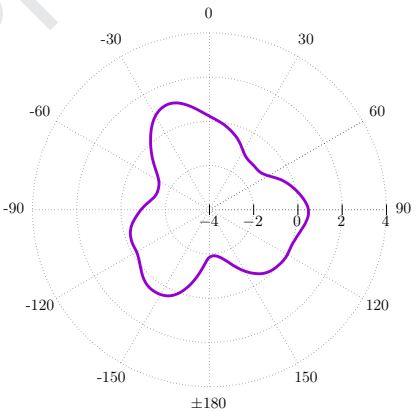

(d) $\widetilde{F_{tot}}$

Figure 15: Polar plots of the phase average of the fluctuating part of the turbine loads $\widetilde{F_{xi}}$, $\widetilde{F_{yi}}$ and $\widetilde{F_{tot}}$, expressed in N, for the turbine in rotation at TSR4. The loads of blades 2 and 3 (for F_{xi} and F_{yi}) have been rephased (adding ±120°) to be in phase with blade 1, to enhance the comparisons.

3.3. Spectral response of the turbine

The turbine response to velocity fluctuations is now studied in the spectral domain. In this section, signals are cut into blocks of 2^n points and a Fast Fourier Transform is applied on every block. For the loads, the acquisition frequency is $f_e = 120\ Hz$ and $n = 12$. The Power Spectral Density S_{FF} of the

turbine loads F_{xi} and F_{tot} are presented in Figure 16 for the parked turbine (**a**) and for the turbine in rotation at TSR4 (**b**).

All presented spectra follow a $-11/3$ power slope. As suggested by Chamorro et al. [35], the turbine power and loads fluctuations are strongly modulated by the structure of the incoming flow in a complex manner. They especially observed a phenomenological relation between the power P and velocity as: $S_{PP}(f) = G(f) \cdot S_{uu}(f)$, where $G(f)$ represents a transfer function. Tobin et al. [36] proposed a power law with a slope of $-11/3$ describing the power spectra of a wind turbine as to be appropriate over the inertial sub-range, where the incoming velocity fluctuates according to the well-known $-5/3$ power low of isotropic turbulence. This was validated with turbine sizes from laboratory models to MW scales. Indeed, they introduced a relation based on the impulse response of the turbine to fluctuations in wind power. As the frequency becomes large, they showed that the power spectrum of this impulse response (i.e. the transfer function $G(f)$) approaches the f^{-2} behaviour. This was later confirmed by the angular velocity spectral behaviour of three different rotating structures (plate with different shapes) by Jin et al. [37], with the same physical description of the phenomenon. This $-11/3$ power law slope of the turbine loads originates from the inertial sub-range of the velocity perceived through the turbine transfer function: $-11/3 = -5/3 - 2$.

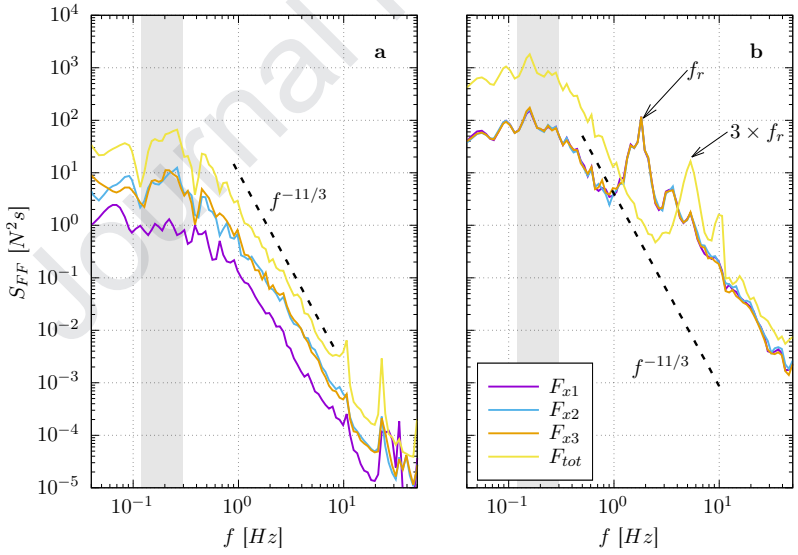

Figure 16: Power Spectral Density S_{FF} of the turbine loads F_{xi} $(i = 1, 2, 3)$ and F_{tot} for the parked turbine (TSR0) **a** and for the turbine in rotation at TSR4 **b**. The largest peak around $f \simeq 0.2\ Hz$ corresponds to the vortex shedding frequency from the cylinder. It is highlighted by the grey area. For the rotating turbine, the rotation frequency is visible at $f_r = 1.8\ Hz$ as well as the blade passing frequency at $3 \times f_r = 5.4\ Hz$. These spectra follow a $-11/3$ power slope.

Other studies, have also reported an excess of energy in the turbine power

spectra in the narrow band around the blade-passing frequency, e.g. [21, 14]. This effect is visible in these results for the rotating turbine (figure 16**b**). The main peak of the F_{tot} spectrum is located at $3 \times f_r = 5.4\ Hz$, i.e. the blade passing frequency. F_{xi} spectra show however a peak at the rotation frequency $f_r = 1.8\ Hz$. They are furthermore all superimposed.

For the parked turbine on the contrary, the amplitude of $S_{F_{x1}F_{x1}}$ is the lowest and the spectra of F_{x2} and F_{x3} are higher and identical. Blades 2 and 3 are indeed fully and always immersed in the turbulent cylinder wake, on the contrary to blade 1. Loads fluctuations are then larger on blades 2 and 3 compared to blade 1. High frequency peaks are visible on all spectra of TSR0 case as well, probably due to mechanical artefacts induced by the speed control system keeping the turbine parked.

One of the novelties brought by this study lies in the high energy and low frequency peak observed around $f \simeq 0.2\ Hz$ for most spectra. It is highlighted by the grey area on figure 16 and corresponds to the vortex shedding frequency, described in Ikhennicheu et al. [25], coming from the upstream wall-mounted cylinder. It is absent on blade 1 spectrum for TSR0 case because blade 1 is never on the vortices trajectories without rotation. Such specific spectra could be observed on a full-scale tidal turbine loads located in the Alderney Race, due to bathymetry variations. According to the loads measured on the turbine model during this experimental campaign, the effects of these low frequency fluctuations could significantly impact operating conditions for real-life marine current turbine.

The coherence function is often used to examine the relation between two signals in the spectral domain. For signals u and F_{tot}, the coherence function is evaluated from their spectra and co-spectra using the following equation:

$$C_{uF_{tot}}(f) = \frac{|S_{uF_{tot}}(f)|^2}{S_{uu}(f) S_{F_{tot}F_{tot}}(f)} \tag{3}$$

Coherence between the velocity and the thrust fluctuations is studied for the turbine at TSR0 and TSR4 in Figure 17. The coherence is elevated, i.e. higher than 0.6, until about $f = 0.6\ Hz$ then falls to 0.1. It is higher than 0.8 in the frequency range of the vortex shedding, i.e. for $f \simeq 0.2\ Hz$, which is highlighted by the grey area on figure 17. The vortices emitted periodically behind the cylinder as well as the low frequency components of the velocity dominate the turbine loads response to velocity fluctuations. The global thrust fluctuations do not respond to the highest frequency velocity fluctuations. That effect is partly assumed to be caused by the turbine active control strategy, which is used to maintain a constant rotation speed. It limits the effect of structures whose frequency is higher than the turbine rotation frequency, as supposed by Durán Medina et al. [38] or Payne et al. [14]. This critical frequency also depends on the turbine size compared to the vortex size. The highest frequencies encountered in the velocity fluctuations are associated with the smallest vortices. Chamorro et al. [35] introduced this critical frequency as $f_c = u_\infty/(D/2) = 2.8\ Hz$ in this case. This frequency is in good agreement

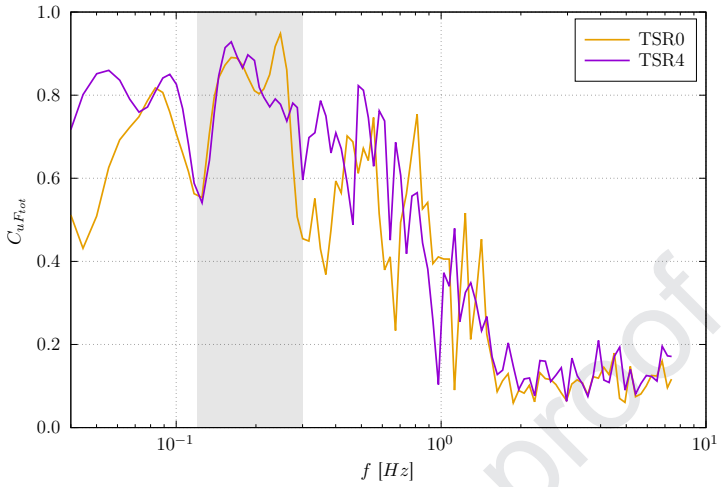

Figure 17: Coherence function $C_{uF_{tot}}$ between the streamise component of the velocity u extracted from the PIV field at $x^* = 15.8$ and $z^* = 4$ and the turbine global thrust F_{tot} when the turbine is parked (TSR0) or in rotation at TSR4. As for figure 16, the narrow band vortex shedding frequency from the cylinder is depicted by the grey area, highlighting the highest values of the coherence function.

with the presented results with the lowest coherence function obtained from $f \geq 1.5\ Hz$. Gaurier et al. [39] described the turbine loads as being insensitive to the vortices with turbulent length scales smaller than the turbine diameter. According to Tobin et al. [36] or Anvari et al. [40] for a single wind turbine, the rotor behaves as a low-pass filter: it ignores the small-scale fluctuations and only responds to larger coherent structures. These observations are confirmed here by the presented results for a tidal turbine submitted to this particular turbulent flow generated from an upstream wall-mounted cylinder.

3.4. Discussion

Gaurier et al. [39] explained it is necessary to measure the upstream velocity to characterize the performance coefficients of a tidal turbine properly, especially when the flow is highly turbulent. It especially limits the uncertainties (which can reach 10 % for the power coefficient, when $I_\infty \simeq 15$ %) from the flow variations and their corresponding time-average values. They proposed an upstream distance of 2 diameters between the velocity measurement and the turbine location. They argued that such distance disables the turbine induction effects on the velocity to be measured. This distance is not too far from the turbine either and enables the velocity fluctuations to be not so different from those perceived by the turbine. These considerations are however only valid for an homogeneous and developed turbulent flow. The flow conditions of this experimental study are particular because the turbulence is mainly generated by a wall-mounted cylinder, located upstream of the turbine. Indeed, Ikhennicheu et al. [23] pointed out the presence of coherent and energetic flow structures

rising up from the cylinder to the surface. On figure 13**a**, we compare the cross-correlation between the turbine thrust and the streamwise velocity measured at two different locations: about 5 cm (with PIV) and 2 diameters (with LDV) upstream from the turbine. This comparison clearly shows that the flow velocity characterization carried out 2 diameters upstream from the turbine is significantly different from the flow velocity perceived by the turbine. Their fluctuating parts are not the same due to:

1. the rising-up nature of the flow behind the obstacle,
2. the different locations of these velocity measurement devices from the obstacle.

Finally, to experimentally quantify the response of this tidal turbine model to such flow velocity fluctuations it is necessary to measure the velocity as close as possible to the turbine. This conclusion is however specific to tidal turbines submitted to that particular flow with turbulence originated from bathymetry variations, like those encountered in the Alderney Race (middle of the English Channel). Durán Medina et al. [13] show for instance a high level of coherence and correlation for an identical tidal turbine model (placed in the same flume tank) submitted to fully developed and homogeneous turbulence with flow measurements carried out 4 diameters upstream from the turbine. In the wind industry, upstream velocity is measured to continuously readjust the turbine's yaw alignment and therefore enhance the turbine's harvested power [41] or to design collective pitch controls to reduce the loads that wind turbines suffer from incoming turbulent gusts [42]. That is why the measurements are usually taken 1 or 2 diameters upstream from the turbine and are then extrapolated to the turbine location using numerical models (Ref. [43] for example). It is necessary to account for the turbine parameters response time which is $5-10$ s according to Mikkelsen et al. [44]. Cortina and Calaf [45] performed large-eddy simulations to explore the effectiveness of detecting turbulent events at different upstream scanning distances (between $D/4$ and $2D$) using wind lidars mounted on the turbines' nacelle. They concluded that the scanning distance should always be the shortest possible in relation with the wind turbine reaction time. This is in agreement with the findings of this study accounting for the fact that the turbine reaction time is not considered in this academic work.

4. Conclusion

In this work, the response of a three-bladed horizontal axis turbine to velocity fluctuations caused by a wall-mounted cylinder has experimentally been investigated. The turbine measurements show that the amplitudes of the loads variation represent about 40 % of their time-average. These amplitudes are furthermore about 6 times higher when the turbine is in rotation at its nominal tip speed ratio compared to when it is parked. Moreover, the velocity shear created when vortices go through the turbine swept area instantaneously increases the fluctuation of these loads at the rotation frequency.

The correlation between the turbine loads and the velocity fluctuations highlights that PIV measurement in the symmetry plane provides a useful tool to quantify the incoming turbulent flow. The angular evolution of the local load shows that the evolution of F_{xi} follows the average velocity profile with a $-30°$ phase delay. According to Gao et al. [46] who recently observed the same phenomenon on a large-scale wind turbine, this phase lag is due to rotational effects. Shen et al. [47] attributed such a phase lag to an asymmetry of wake structure of the blade. Load spectral analysis enables two peaks to be extracted: at the blade passing frequency and at the vortex shedding frequency. Each Power Spectral Density follows a $-11/3$ power slope in the inertial sub-range, where the incoming velocity fluctuates according to the well-known -5/3 power law. This confirms the -2 power slope of the turbine transfer function, introduced by Chamorro et al. [35] and its phenomenological description by Tobin et al. [36]. The coherence function between the velocity and the turbine loads shows a peak in the frequency range of the vortex shedding. This illustrates that the turbulent structures emitted in the cylinder wake predominate on the turbine response. The coherence study also shows that the turbine does not respond to high frequency fluctuations, i.e. when frequencies are higher than 1 Hz. Hence, the coherent and energetic wake coming from a wall-mounted cylinder induces intense and periodic loads fluctuations on the turbine. Those results illustrate the importance of considering velocity fluctuations from bathymetry fluctuations when studying a turbine behaviour in realistic conditions.

To complete this work, it would be interesting to test other distances between the turbine and the obstacle to see the evolution of the turbine response when it is progressively immersed in the cylinder wake. This database is available on the Seanoe platform [48] and can be used for blade and rotor fatigue analysis.

Acknowledgment

This work benefits from a French State grant managed by the National Research Agency under the Investments for the Future program bearing the reference ANR-10-IEED-0006-11. This work also received the support of the Met-Certified project, funding from the Interreg 2 Seas programme 2014-2020, co-funded by the European Regional Development Fund under subsidy contract N. 2S01-020. This project was partly financially supported by the European Union (FEDER), the French government, IFREMER and the region Hauts-de-France in the framework of the project CPER 2015–2020 MARCO. The authors also acknowledge the financial support of IFREMER and the Hauts de France Regional Council for the PhD study of Maria Ikhennicheu. We are most grateful to Thomas Bacchetti, Inès Belarbi and Jean-Valery Facq for their assistance and precious advices.

[1] B. Gaurier, P. Davies, A. Deuff, G. Germain, Flume tank characterization of marine current turbine blade behaviour under current and wave loading, Renewable Energy 59 (2013) 1–12. doi:10.1016/j.renene.2013.02.026.

[2] P. W. Galloway, L. E. Myers, A. B. S. Bahaj, Quantifying wave and yaw effects on a scale tidal stream turbine, Renewable Energy 63 (2014) 297–307. doi:10.1016/j.renene.2013.09.030.
URL http://dx.doi.org/10.1016/j.renene.2013.09.030

[3] E. Fernandez-Rodriguez, T. J. Stallard, P. K. Stansby, Experimental study of extreme thrust on a tidal stream rotor due to turbulent flow and with opposing waves, Journal of Fluids and Structures 51 (2014) 354–361. doi:10.1016/j.jfluidstructs.2014.09.012.
URL http://dx.doi.org/10.1016/j.jfluidstructs.2014.09.012

[4] R. Martinez, G. S. Payne, T. Bruce, The effects of oblique waves and currents on the loadings and performance of tidal turbines, Ocean Engineering 164 (June) (2018) 55–64. doi:10.1016/j.oceaneng.2018.05.057.
URL https://doi.org/10.1016/j.oceaneng.2018.05.057

[5] S. Draycott, G. Payne, J. Steynor, A. Nambiar, B. Sellar, V. Venugopal, An experimental investigation into non-linear wave loading on horizontal axis tidal turbines, Journal of Fluids and Structures 84 (2019) 199–217. doi:10.1016/j.jfluidstructs.2018.11.004.
URL https://doi.org/10.1016/j.jfluidstructs.2018.11.004

[6] S. Ordonez-Sanchez, M. Allmark, K. Porter, R. Ellis, C. Lloyd, I. Santic, T. O'Doherty, C. Johnstone, Analysis of a Horizontal-Axis Tidal Turbine Performance in the Presence of Regular and Irregular Waves Using Two Control Strategies, Energies 12 (3) (2019) 367. doi:10.3390/en12030367.

[7] K. E. Porter, S. E. Ordonez-Sanchez, R. E. Murray, M. Allmark, C. M. Johnstone, T. O'Doherty, A. Mason-Jones, D. A. Doman, M. J. Pegg, Flume testing of passively adaptive composite tidal turbine blades under combined wave and current loading, Journal of Fluids and Structures 93 (2020) 102825. doi:10.1016/j.jfluidstructs.2019.102825.
URL https://doi.org/10.1016/j.jfluidstructs.2019.102825

[8] P. Ouro, T. Stoesser, Impact of Environmental Turbulence on the Performance and Loadings of a Tidal Stream Turbine, Flow, Turbulence and Combustion 102 (3) (2019) 613–639. doi:10.1007/s10494-018-9975-6.

[9] P. Mycek, B. Gaurier, G. Germain, G. Pinon, E. Rivoalen, Experimental study of the turbulence intensity effects on marine current turbines behaviour. Part I: One single turbine, Renewable Energy 66 (2014) 729–746. doi:10.1016/j.renene.2013.12.036.
URL http://dx.doi.org/10.1016/j.renene.2013.12.036https://linkinghub.elsevier.com/retrieve/pii/S096014811400007X

[10] N. D. Kelley, Turbulence descriptors for scaling fatigue loading spectra of wind turbine structural components, in: International Energy Agency Meeting on Wind Conditions for Wind Turbine Design, no. July, Hamburg, Germany, 1994.

[11] M. J. Churchfield, S. Lee, J. Michalakes, P. J. Moriarty, A numerical study of the effects of atmospheric and wake turbulence on wind turbine dynamics, Journal of Turbulence 13 (May) (2012) 1–32. doi:10.1080/14685248.2012.668191.

[12] T. Blackmore, L. E. Myers, A. S. Bahaj, Effects of turbulence on tidal turbines: Implications to performance, blade loads, and condition monitoring, International Journal of Marine Energy 14 (2016) 1–26. doi:10.1016/j.ijome.2016.04.017.
URL http://dx.doi.org/10.1016/j.ijome.2016.04.017

[13] O. Durán Medina, F. G. Schmitt, R. Calif, G. Germain, B. Gaurier, Turbulence analysis and multiscale correlations between synchronized flow velocity and marine turbine power production, Renewable Energy 112 (2017) 314–327. doi:10.1016/j.renene.2017.05.024.

[14] G. S. Payne, T. Stallard, R. Martinez, T. Bruce, Variation of loads on a three-bladed horizontal axis tidal turbine with frequency and blade position, Journal of Fluids and Structures 83 (2018) (2018) 156–170. doi:10.1016/j.jfluidstructs.2018.08.010.
URL https://doi.org/10.1016/j.jfluidstructs.2018.08.010

[15] T. Blackmore, B. Gaurier, L. Myers, G. Germain, A. S. Bahaj, The Effect of Freestream Turbulence on Tidal Turbines, in: Proceedings of the 11th European Wave and Tidal Energy Conference, Nantes, France, 2015.

[16] P. Davies, G. Germain, B. Gaurier, A. Boisseau, D. Perreux, Evaluation of the durability of composite tidal turbine blades, Philosophical Transactions of the Royal Society A: Mathematical, Physical and Engineering Sciences 371 (1985) (2013) 20120187. doi:10.1098/rsta.2012.0187.
URL https://royalsocietypublishing.org/doi/10.1098/rsta.2012.0187

[17] M. Lewis, J. McNaughton, C. Márquez-Dominguez, G. Todeschini, M. Togneri, I. Masters, M. Allmark, T. Stallard, S. Neill, A. Goward-Brown, P. Robins, Power variability of tidal-stream energy and implications for electricity supply, Energy 183 (2019) 1061–1074. doi:10.1016/j.energy.2019.06.181.

[18] P. H. Madsen, K. Pierce, M. Buhl, Predicting ultimate loads for wind turbine design, in: 37th Aerospace Sciences Meeting and Exhibit, no. November 1998, Reno, Nevada, 1999, pp. 355–364. doi:10.2514/6.1999-69.

[19] L. P. Chamorro, C. Hill, V. S. Neary, B. Gunawan, R. E. A. Arndt, F. Sotiropoulos, Effects of energetic coherent motions on the power and wake of an axial-flow turbine, Physics of Fluids 27 (5). doi:10.1063/1.4921264.
URL http://dx.doi.org/10.1063/1.4921264

[20] R. Byrne, N. J. Hewitt, P. Griffiths, P. MacArtain, Observed site obstacle impacts on the energy performance of a large scale urban wind turbine using an electrical energy rose, Energy for Sustainable Development 43 (2018) 23–37. doi:10.1016/j.esd.2017.12.002.

[21] L. P. Chamorro, C. Hill, S. Morton, C. Ellis, R. E. A. Arndt, F. Sotiropoulos, On the interaction between a turbulent open channel flow and an axial-flow turbine, Journal of Fluid Mechanics 716 (2013) 658–670. doi:10.1017/jfm.2012.571.

[22] T. Suzuki, H. Mahfuz, Fatigue characterization of GFRP and composite sandwich panels under random ocean current loadings, International Journal of Fatigue 111 (November 2017) (2018) 124–133. doi:10.1016/j.ijfatigue.2018.02.004.
URL https://doi.org/10.1016/j.ijfatigue.2018.02.004

[23] M. Ikhennicheu, G. Germain, P. Druault, B. Gaurier, Experimental investigation of the turbulent wake past real seabed elements for velocity variations characterization in the water column., International Journal of Heat and Fluid Flow 78 (June) (2019) 108426. doi:10.1016/j.ijheatfluidflow.2019.108426.
URL https://doi.org/10.1016/j.ijheatfluidflow.2019.108426https://linkinghub.elsevier.com/retrieve/pii/S0142727X18311925

[24] L. Furgerot, Y. Poprawski, M. Violet, E. Poizot, P. Bailly du Bois, M. Morillon, Y. Mear, High-resolution bathymetry of the Alderney Race and its geological and sedimentological description (Raz Blanchard, northwest France), Journal of Maps 15 (2) (2019) 708–718. doi:10.1080/17445647.2019.1657510.

[25] M. Ikhennicheu, G. Germain, P. Druault, B. Gaurier, Experimental study of coherent flow structures past a wall-mounted square cylinder, Ocean Engineering 182 (May) (2019) 137–146. doi:10.1016/j.oceaneng.2019.04.043.

[26] C. D. Meinhart, A. K. Prasad, R. J. Adrian, A parallel digital processor system for particle image velocimetry, Measurement Science and Technology 4 (5) (1993) 619–626. doi:10.1088/0957-0233/4/5/013.

[27] J. Westerweel, F. Scarano, Universal outlier detection for PIV data, Experiments in Fluids 39 (6) (2005) 1096–1100. doi:10.1007/s00348-005-0016-6.

[28] B. Gaurier, G. Germain, J.-V. Facq, Experimental study of the Marine Current Turbine behaviour submitted to macro-particle impacts, in: Proceedings of the 12th European Wave and Tidal Energy Conference, Cork, Ireland, 2017.

[29] B. Gaurier, G. Germain, J.-V. V. Facq, C. M. Johnstone, A. D. Grant, A. H. Day, E. Nixon, F. Di Felice, M. Costanzo, Tidal energy "round Robin" tests comparisons between towing tank and circulating tank results, International Journal of Marine Energy 12 (2015) 87–109. doi:10.1016/j.ijome.2015.05.005.
URL http://dx.doi.org/10.1016/j.ijome.2015.05.005

[30] B. Gaurier, G. Germain, J.-V. Facq, T. Bacchetti, Wave and current flume tank of IFREMER at Boulogne-sur-mer. Description of the facility and its equipment, Tech. rep., Ifremer (2018). doi:10.13155/58163.

[31] L. Li, Y. Liu, Z. Yuan, Y. Gao, Wind field effect on the power generation and aerodynamic performance of offshore floating wind turbines, Energy 157 (2018) 379–390. doi:10.1016/j.energy.2018.05.183.
URL https://doi.org/10.1016/j.energy.2018.05.183

[32] E. Simley, N. Angelou, T. Mikkelsen, M. Sjöholm, J. Mann, L. Y. Pao, Characterization of wind velocities in the upstream induction zone of a wind turbine using scanning continuous-wave lidars, Journal of Renewable and Sustainable Energy 8 (1). doi:10.1063/1.4940025.
URL http://dx.doi.org/10.1063/1.4940025

[33] A. Mason-Jones, D. M. O'Doherty, C. E. Morris, T. O'Doherty, Influence of a velocity profile & support structure on tidal stream turbine performance, Renewable Energy 52 (2013) 23–30. doi:10.1016/j.renene.2012.10.022.

[34] J. C. Dai, Y. P. Hu, D. S. Liu, X. Long, Aerodynamic loads calculation and analysis for large scale wind turbine based on combining BEM modified theory with dynamic stall model, Renewable Energy 36 (3) (2011) 1095–1104. doi:10.1016/j.renene.2010.08.024.

[35] L. P. Chamorro, S.-J. Lee, D. Olsen, C. Milliren, J. Marr, R. Arndt, F. Sotiropoulos, Turbulence effects on a full-scale 2.5 MW horizontal-axis wind turbine under neutrally stratified conditions, Wind Energy 18 (2) (2015) 339–349. doi:10.1002/we.1700.
URL http://doi.wiley.com/10.1002/we.1700

[36] N. Tobin, H. Zhu, L. P. Chamorro, Spectral behaviour of the turbulence-driven power fluctuations of wind turbines, Journal of Turbulence 16 (9) (2015) 832–846. doi:10.1080/14685248.2015.1031242.
URL http://www.tandfonline.com/doi/full/10.1080/14685248.2015.1031242

[37] Y. Jin, S. Ji, L. P. Chamorro, Spectral energy cascade of body rotations and oscillations under turbulence, Physical Review E 94 (6) (2016) 063105. doi:10.1103/PhysRevE.94.063105.
URL https://link.aps.org/doi/10.1103/PhysRevE.94.063105